Effects of Zn/Al mass ratio on microstructure evolution and mechanical properties of Mg-Sn based alloys

Yuxiao Luo [a], Yu'an Chen [a, b, *], Lei Ran [a], Xu Pang [a], Fusheng Pan [a, b]

[a] College of Materials Science and Engineering, Chongqing University, Chongqing 400044, China

[b] National Engineering Research Center for Magnesium Alloys, Chongqing University, Chongqing 400044, China

Abstract: Effects of Zn/Al mass ratio on the microstructure evolution and mechanical properties of the Mg-3Sn-5Zn-xAl (x=0,1,2,3 wt.%) alloy were systematically investigated in the present study. The secondary phases of as-cast alloys were transformed from $MgZn_2$/α-Mg eutectics and Mg_2Sn to icosahedral (I-) phase and Mg_2Sn with decreasing of Zn/Al mass ratio. After extrusion, almost completely recrystallized fine grains were obtained in TZ35-xAl alloys, but the volume fraction of recrystallized region was slightly reduced by the addition of Al. This phenomenon was chiefly ascribed to the particle-stimulated nucleation (PSN) mechanism and Zener grain-boundary pinning effect induced by enormous numbers of fine Mg-Zn phase, I-phase, Mg_2Sn and newly formed φ-phase (related to I-phase) particles. As-extruded alloys exhibited superior strength and ductility balance. Specifically, Mg-3Sn-5Zn-1Al alloy got the highest ultimate tensile strength and elongation, reaching 340 MPa and 20.1%, respectively. Moreover, tensile yield strength of as-extruded alloys rises dramatically from 169 MPa to 212 MPa along with rising of the Al level. Improved tensile yield strength is primarily attributed to the synergistic reinforcement mechanism of grain refinement and dynamic precipitation of fine secondary particles. The excellent ductility for all as-extruded alloys owes a great deal to the activation of non-basal slip systems, high volume fraction of fine DRXed grains and weakened texture.

Keywords: Mg-Sn-Zn-Al alloys, microstructure evolution, I-phase, dynamic recrystallization, mechanical properties.

*Corresponding author.
Telephone number: +8613368002893.
E-mail address: chenyuan@cqu.edu.cn (Yu'an Chen).

1.Introduction

As the lightest commercial structural material, magnesium alloys possess superior properties such as outstanding damping performance, high specific strength, recyclability and rich resources, and are acclaimed as the green engineering material in the 21st century. It has wide-ranging prospects in aerospace, automobile industry, 3C and so forth [1, 2]. However, low strength, poor plasticity and inferior high temperature mechanical properties limit the wide application of magnesium alloys in some industrial fields [3].

In recent years, extensive researches have focused on improving the mechanical properties of commercial Mg-Zn [4] and Mg-Al based alloys [5] by grain refinement and improving age hardening effect. However, the thermally unstable β-$Mg_{17}Al_{12}$ and Mg-Zn phases with low melting temperature make Mg-Zn and Mg-Al based alloys exhibit poor extrudability and creep resistance. Mg-RE (RE means rare earth elements) based alloys [6] display excellent thermal stability and precipitation strengthening effect. But recent issues such as the lack of resources and rising prices further restrict the extensive utilization of Mg-RE alloys in industry. In Mg-Sn based alloys, Mg_2Sn has high thermal stability comparable to precipitates in Mg-RE alloys, which can effectively hinder the growth of dynamically recrystallized grains during extrusion. Moreover, the Sn element is comparatively cheap, and its solid solubility in Mg matrix varies greatly with temperature [7, 8]. Therefore, Mg-Sn based alloys with superior extrudability and precipitation hardening effect have gradually become a proper candidate in the development of cost-effective high strength magnesium alloys. Nevertheless, related research shows that Mg_2Sn is easy to coarsen and grow up quickly in Mg-Sn binary alloy, which would worsen the mechanical properties of the Mg alloy [9, 10].

Zn and Al are the essential alloying elements in Mg-Sn based alloys. Addition of Zn not only promotes the age hardening response of Mg-Sn based alloy, but also refines the Mg_2Sn particles [11]. Al can improve the castability, weaken the texture and ameliorate the plasticity of the alloy [12, 13]. When Zn and Al are added at the same time, different Zn/Al mass ratio may produce different types of secondary phase. Traditional commercial high-strength alloy such as AZ61 and AZ91 [14, 15] would soften above 120°C due to the formation of β-$Mg_{17}Al_{12}$ phase. In view of previous studies [16-19], when the mass fraction of Zn is more than 2% and the mass ratio of Zn/Al is greater than 1, thermostable τ-$Mg_{32}(Al, Zn)_{49}$ with relatively high melting temperature instead of β-$Mg_{17}Al_{12}$ would be formed. S. Harosh et al. [20] discovered that $Mg_{32}(Al, Zn)_{49}$ and Mg_2Sn in Mg-5.6Sn-4.4Zn-2.1Al (wt.%) was maintained for 32 days at 498 K, and the hardness stably maintained at 56HV. In addition, Takeuchi et al. [21, 22] found a quasi-crystalline phase with composition near $Mg_{44}Zn_{41}Al_{15}$ in Mg-Zn-Al alloys, which exhibited excellent thermal stability.

I-phase has been well known to form based on the Frank-Kasper τ-$Mg_{32}(Al, Zn)_{49}$ phase with a body-centered cubic structure (space group Im3, a≈1.4 nm) in Mg-Zn-Al alloy system [23-26]. Some researchers argued that I-phase is a kind of metastable phase, and it transforms into the equilibrium cubic τ-$Mg_{32}(Al, Zn)_{49}$ phase or equilibrium φ-$Mg_5Al_2Zn_2$ phase with a primitive orthorhombic structure (a=0.8979 nm, b=1.6988 nm, and c=1.9340 nm) [26] when the temperature rases to a certain value [27, 28]. Simultaneously, they have found that there is a great similarity in the structure between τ-phase and I-phase. The body-centered cubic τ-phase is made up of large icosahedral atomic clusters [25, 29], which also have been identified in I-phase structure [30]. In addition, some researches indicate that Mg-Sn-Zn-Al alloy containing I-phase exhibited excellent strength. Kim et al. [22] stated that the yield strength of the as-rolled Mg-7Sn-5Zn-2Al alloy reached 318MPa due to finely dispersed Mg_2Sn and I-phase particles distributed in the matrix.

Up to now, however, few reports have systematically discussed the evolution of the secondary phase in as-cast and as-extruded Mg-Sn-Zn-Al alloys by adjusting the mass ratio of Zn/Al. In the present work, therefore, Mg-3Sn-5Zn-xAl (x =0,1,2,3 wt.%) was designed to understand the effects of Zn/Al mass ratio on the evolution of microstructure and mechanical properties of the Mg-Sn-Zn-Al alloy, aiming to form I- or approximant ternary phases with high thermal stability and fine dispersed Mg_2Sn. This study systematically investigated I- or approximant ternary phases in this system, and tried to explore the orientation relationship between I- or approximant ternary phase, Mg_2Sn and α-Mg matrix. Simultaneously, the effects of Al on the texture, dynamic recrystallization behaviors and mechanical properties in as-extruded alloys were also discussed in detail.

2.Materials preparation and experimental procedure

In this work, the Mg-3Sn-5Zn-xAl (x=0,1,2,3wt.%, afterward) alloys (named TZ35, TZA351, TZA352, TZA353) were prepared from commercial Mg, Al, Sn and Zn block (with high purity of 99.98wt.%). The melting experiment was conducted using a resistance furnace with a low carbon steel crucible at 720°C under the protection of CO_2 and SF_6 mixed gas atmosphere. After uniformly mixed, the molten alloy was poured into a previously preheated mould (preheating temperature was 300°C), and then followed by air cooling at room temperature to get a cast ingot with the size of φ74mm and height of 200mm. Homogenization treatment was then carried out at 330°C for 25h in a SX-2.5-12 resistance furnace followed by air cooling in order to eliminate defects and element segregation in as-cast alloys, which would be beneficial to subsequent hot working deformation. The homogenized billets (φ 69 mm, height 100 mm) were preheated at 300°C for 0.5 h, and then extruded into 16 mm diameter rods in XJ-500 horizontal extruder at a relatively low temperature of 300°C with a ratio of 18.6, and the extrusion speed range from 1m/min to 2m/min.

The X-ray fluorescence spectrophotometer (XRF-1800CCDE) was employed to measure the actual chemical composition of the as-cast alloys, and the results are shown in Table 1. Microstructure characterization of the alloys was performed using the optical microscope (OM, Axiovert 40 MAT), the scanning electron microscope (SEM, TM4000Plus II, Quattro S, TESCAN VEGA3) equipped with an energy dispersive X-ray spectrometer (EDS) and an Oxford Aztec EBSD detector, the transmission electron microscopy (TEM, FEI Talos F200S G2), and X-ray diffractometer (XRD, Rigaku D/max-2500 PC). OM and SEM samples were etched with 3% and 4% (volume fraction) nitric acid solution before observation in order to show the grain structure. Phase composition of the alloys was identified by an X-ray diffraction (XRD) instrument with Cu-Ka and a scanning rate of 4/min on the scanning angles between 10°and 90°. Ultrathin TEM samples were prepared by manually grinding to acquire a foil about 50μm, and then followed by ion beam thinning using Gatan695 low temperature ion thinning apparatus. 5×5×3mm specimens for EBSD experiment were cut along the extrusion direction (ED) from extrusion rods. Soon afterwards, these samples were ground to mirror-like surfaces without obvious scratches, and then followed by ion polishing in ACII solution for approximately 150s. EBSD analysis was performed on a scanning electron microscope (JEOL 7800F) equipped with an HKL Channel 5 software. In addition, Image-Pro Plus 6.0 software was utilized to measure the volume fraction of the secondary phase and mean spacing of α-Mg dendrite.

Nominal composition（*wt.%*）	Alloy	Measured composition（*wt.%*）			
		Mg	Sn	Zn	Al
Mg-3Sn-5Zn	TZ35	Bal.	3.27	4.74	-
Mg-3Sn-5Zn-1Al	TZA351	Bal.	3.25	4.78	0.92
Mg-3Sn-5Zn -2Al	TZA352	Bal.	3.29	4.80	1.79
Mg-3Sn-5Zn -3Al	TZA353	Bal.	3.34	4.67	2.64

Table 1 The designation and chemical composition of the as-cast alloy.

The room temperature mechanical properties were carried out on a CMT-5105 electronic universal material testing machine with a strain rate of 10^{-3} s^{-1}. Specimens for tensile test with the gauge length of 30mm and diameter of φ5mm were machined from the extruded rods. Three sets of parallel tensile experiments were performed for each alloy to obtain average values.

3.Results and discussion

3.1 Microstructure and phase identification of as-cast alloys

Fig. 1 gives the OM images of the as-cast TZ35-xAl alloys. All the microstructure of as-cast alloys is composed of a typical dendrite structure and intergranular compounds. With the increasing of Al content, the secondary dendrite spacing of α-Mg reduced from 37.4μm in TZ35 to 20.2μm in TZA353, and the dendrite morphology tends to transform into a round rosette. Moreover, intergranular secondary phases present a network distribution and the volume fraction increase from 1.90% to 2.91% with the addition of Al.

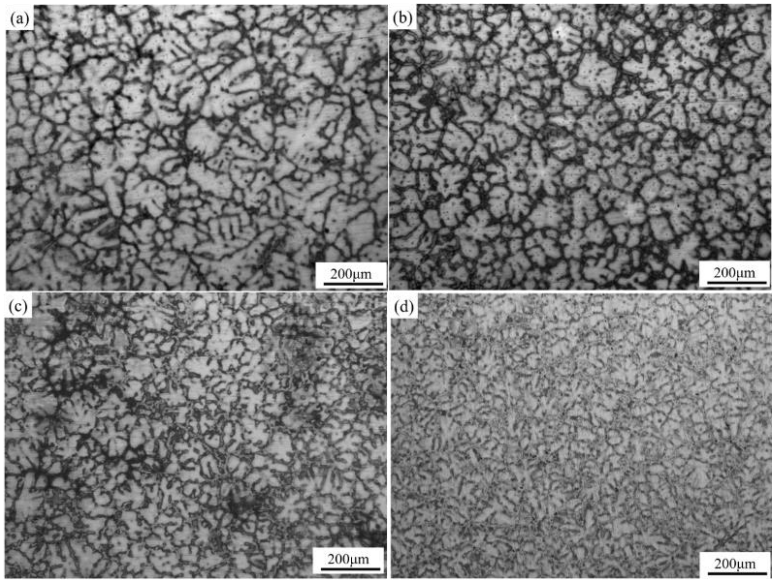

Fig. 1. Optical micrographic images of as-cast Mg-3Sn-5Zn-xAl alloys: (a) x=0, (b) x=1 (c) x=2 (d) x =3.

In order to identify the phase composition and clearly observe the morphology of the secondary phase in as-cast alloys, the SEM images and XRD pattern of as-cast alloys were exhibited in Fig. 2, respectively, and the EDS results corresponding to SEM photos were also given in Table 2. As seen

from Fig. 2a and corresponding EDS results in Table 2, the intergranular compounds of TZ35 alloy consist of Mg-Zn/α-Mg eutectics with dark contrast and Mg_2Sn phase with bright contrast, the two kinds of phases tend to grow on each other. Similar results can be observed in the research of Wang et al. [31]. With the addition of Al element, the second phase of the alloy transformed from a block-like phases to a continuous distribution of fishbone-like second phases. In the light of the EDS results, the fishbone-like phase is the Mg-Zn-Al ternary phase. Combined with the XRD pattern, it can be concluded that the as-cast TZ35-xAl alloys includes primary α-Mg, $MgZn_2$, I-phase (which was confirmed by subsequent STEM analysis) and Mg_2Sn phase. As expected, the diffraction peak of β-$Mg_{17}Al_{12}$ phase is not found in XRD pattern. Obviously, the addition of Al led to the transformation of the type of the second phase in as-cast TZ35-xAl alloys, that is, from $MgZn_2$/α-Mg eutectics to I-phase. It is considered that the addition of Al preferentially formed Mg-Zn-Al ternary phase with Mg and Zn atoms, which consumed the content of Zn in the alloy, resulting in decreasing levels of $MgZn_2$ phase. Although the addition of Al did not affect the chemical composition and physical structure of Mg_2Sn, which is the main phase of Mg-Sn based alloys, it may lead to reducing the solid solubility of Sn atoms in the α-Mg matrix, and promoting the precipitation of Mg_2Sn [12]. Therefore, diffraction peak intensity of the Mg_2Sn in XRD pattern increases slightly along with the rising of the Al level. Significantly, the diffraction peaks of I-phase in XRD pattern correspond to those of τ-phase $Mg_{32}(Al, Zn)_{49}$ on account of great similarity in the cell structure between τ-phase and I-phase [25].

Alloy	Points	Element (at.%)				Phase
		Mg	Sn	Zn	Al	
Mg-3Sn-5Zn	A	70.61	29.39	-	-	Mg_2Sn
	B	73.97	-	26.03	-	$MgZn_2$
Mg-3Sn-5Zn-1Al	C	69.10	5.06	25.84	-	$MgZn_2$+ Mg_2Sn
	D	70.57	-	24.85	4.58	$MgZn_2$+I-phase
Mg-3Sn-5Zn-2Al	E	49.27	-	33.86	16.87	I-phase
	F	54.56	-	31.14	14.30	I-phase
Mg-3Sn-5Zn-3Al	G	58.52		22.39	19.09	I-phase
	H	56.85	-	24.59	18.56	I-phase

Table 2 Corresponding EDS results of as-cast alloys in Fig. 2 SEM images.

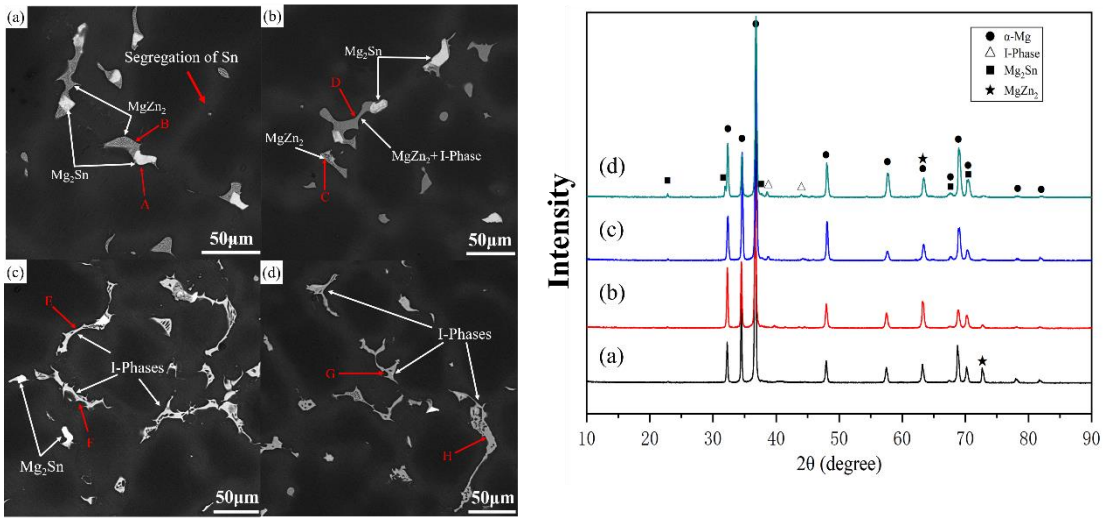

Fig. 2. SEM images and XRD patterns of as-cast TZ35-xAl alloys: (a) x=0, (b) x=1 (c) x=2 (d) x =3.

TEM analysis for as-cast TZA353 alloy is given in Fig. 3-4, which can help us further identifying the crystal structure of the ternary Mg-Zn-Al phase in this alloy system. Low amplification STEM image (Fig. 3a) shows an irregular phase with a size of about 7μm, and corresponding surface scanning elements distribution (Fig. 3b) indicates that this precipitate is a Mg-Zn-Al ternary phase. Selected area electron diffraction pattern (Fig. 3c) obtained from the red circle position in Fig. 3a reveals that the diffraction spots of the ternary phase do not have the same translational periodicity as the crystal structure, such as that in a body-centered cubic τ-phase. By contrary, the pattern presents a quasi-crystalline structure oriented along the twofold rotational symmetry axis [2-fold]$_I$. Similar diffraction pattern can be observed in the literature [27], but the diffraction pattern in Fig. 3c is more complex than that in the previous research, which seems to be the result of secondary diffraction.

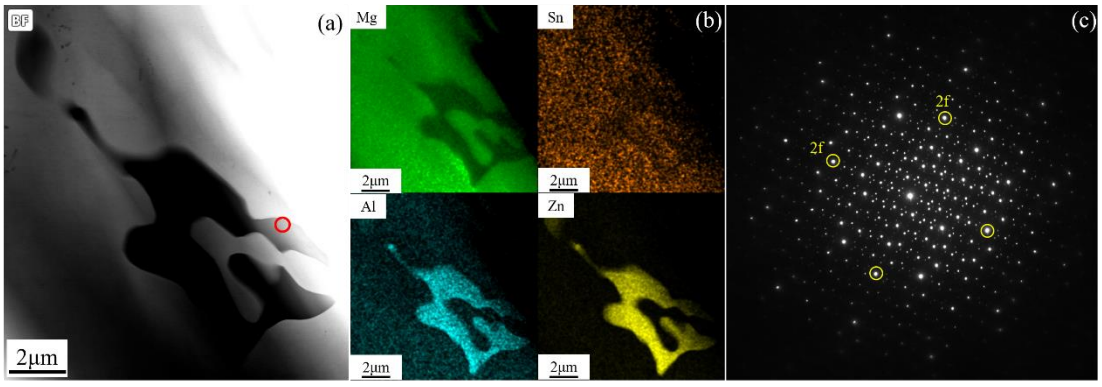

Fig. 3. (a) Bright field STEM image show an irregular I-phase taken from the [2-fold]$_I$ zone axis; (b) EDS mapping of this precipitate; (c) Corresponding selected area electron diffraction (SAED) pattern.

In addition, Fig. 4a shows a high magnification STEM image of another rhombic particle with a size of 60nm in TZA353 alloy, which has been identified as Mg-Zn-Al quasi-crystalline I-phase

with a typical threefold rotational symmetry structure by SAED in Fig. 4b and corresponding EDS mapping analysis in Fig. 4c. Interestingly, we found that this particle precipitated along the grain boundary, and there are a large number of dislocations (marked by the yellow arrow in Fig. 4a) disappearing at the grain boundary near the particle. It can be inferred that these particles and grain boundaries may hinder the motion of dislocations during deformation, thus improving the mechanical properties of the alloys. The SAED pattern corresponding to the area (red circle marked in Fig. 4a) between the particle and surrounding α-Mg matrix reveal that there is a certain orientation relationship between matrix and I-phase. The orientation relationship can be expressed as follows: $[3\text{-fold}]_I//[0001]_\alpha$ and $(3f)_I//\{11\bar{2}0\}_\alpha$. Previous research also reported the similar orientation relationship between I-phase and α-Mg matrix in Mg-Sn-Zn-Al as-rolled alloy, namely:$[2\text{-fold}]_I//[0001]_\alpha$ and $(2f,5f)_I//\{10\bar{1}0\}_\alpha$ [22].

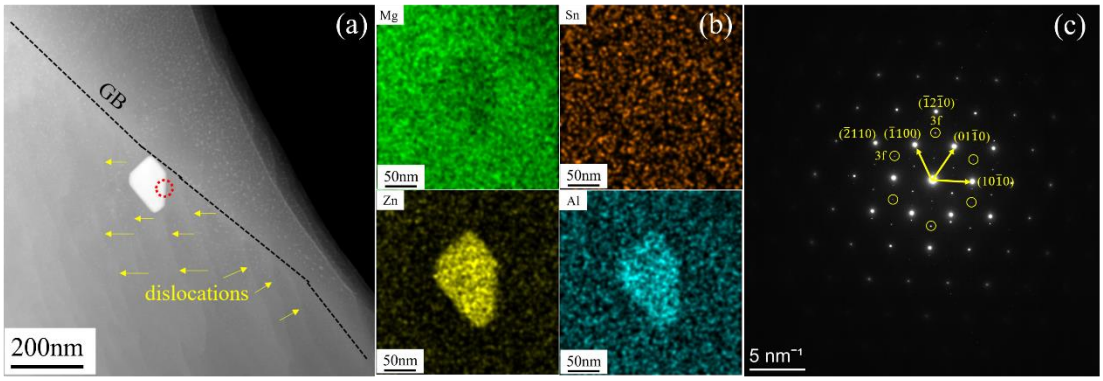

Fig. 4. STEM image of the TZA353 alloy. (a) shows an I-phase particle and nearby dislocations with electron beam parallel to [0001] $_{Mg}$ zone axis; (b) EDS mapping this particle; (c) corresponding selected area electron diffraction (SAED) pattern.

3.2 Microstructure of as-homogenized alloys

Homogenization treatment was carried out in order to eliminate defects and element segregation in as-cast alloys, which would be beneficial to subsequent hot working deformation. The SEM and EDS analysis results of as-homogenized TZ35, TZA352 and TZA353 alloys are presented in Fig. 5. Only a small amount of Mg_2Sn phases with a high melting temperature (770°C) remained in TZ35 alloy, and Mg-Zn/α-Mg eutectic phases almost dissolved into the matrix. Compared with TZ35 alloy, residual Mg-Zn-Al ternary phases were found in TZ35-xAl (x=2,3) alloy, indicating that Mg-Zn-Al ternary phases possess excellent thermal stability. Those coarse residual secondary phase would be brittlely crushed into streamlined fragments during the subsequent hot extrusion process, which may greatly promote the DRX behavior of as-extruded alloys.

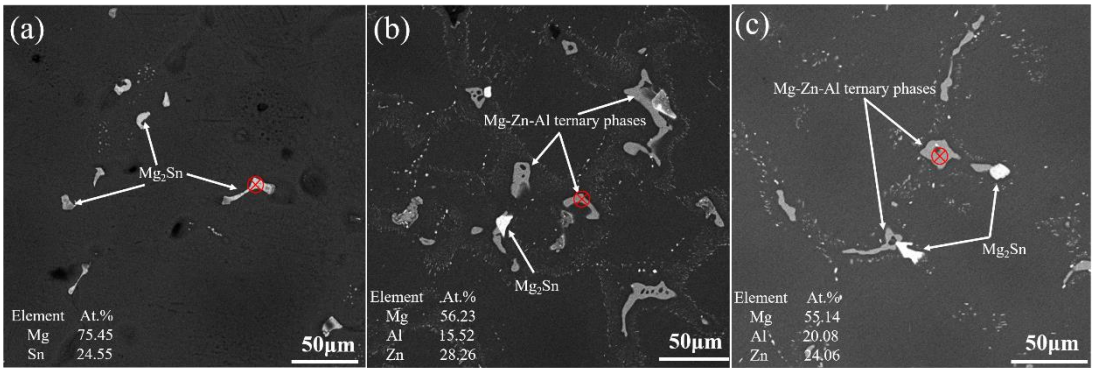

Fig. 5. SEM micrographs and corresponding EDS results of residual secondary phases in as-homogenized alloys: (a) TZ35, (b) TZA352, (c) TZA353.

3.3 Microstructure and EBSD analysis of as-extruded alloys

Fig. 6 illustrated the XRD pattern of as-extruded TZ35-xAl alloys. Compared with the as-cast alloy, obviously, no significant discrepancy appeared in the types of the second phase. As-extruded Al-free alloy is mainly made up of α-Mg, Mg_2Sn and Mg-Zn phases, whereas the Mg-Zn phases are gradually replaced by I-phase in Al-containing alloys with the increase of Al content.

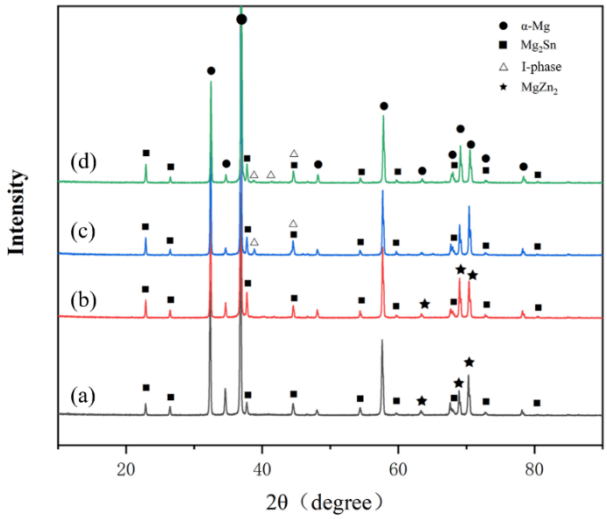

Fig. 6. The XRD patterns of as-extruded TZ35-xAl alloys: (a) x=0, (b) x=1 (c) x=2 (d) x =3.

Fig. 7 shows the low and high magnification SEM micrographs of as-extruded alloys taken along the longitudinal direction. In TZ35 alloy, only a small number of undissolved Mg-Zn phases are elongated or crushed during extrusion, and present streamline distribution along the extrusion direction, while abundant fine lath-like Mg-Zn and Mg_2Sn particles precipitate dynamically and uniformly disperse in the matrix. When 1wt.% Al is added, the volume fraction of dynamically precipitated fine particles increases during the extrusion process, as presented in Fig. 7c-d. However, continuous addition of Al content up to 2-3wt.% leads to coarsening of the I phase and Mg_2Sn, as shown in Fig. 7e-h, which would be harmful to the mechanical properties of as-extruded alloys.

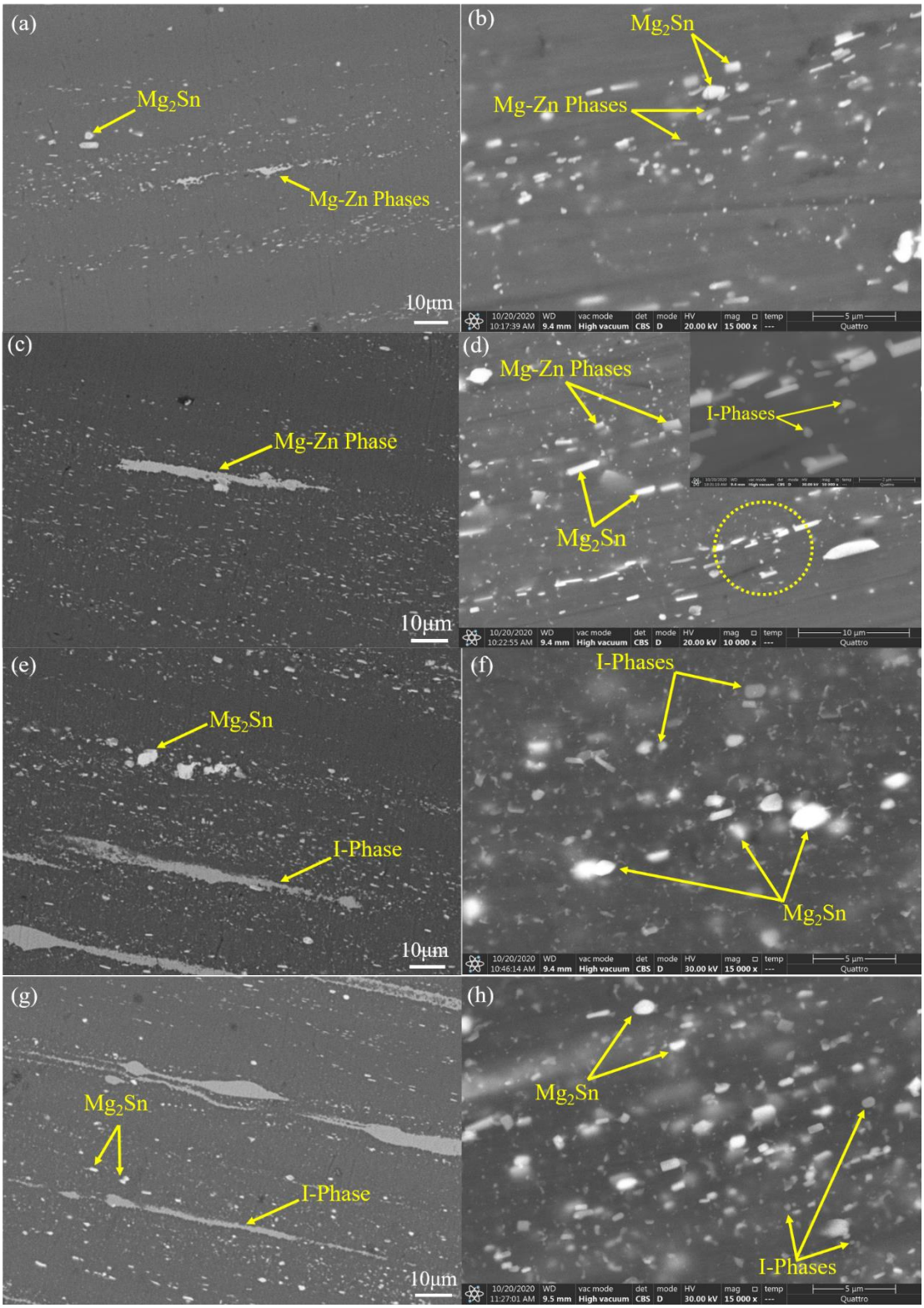

Fig. 7. The Low and high magnification SEM images of as-extruded TZ35-xAl alloys microstructure taken along the extrusion direction (ED): (a-b) x=0; (c-d) x=1; (e-f) x=2; (g-h) x=3.

STEM analysis was conducted to further understand the precipitation evolution of the TZA353 alloy during extrusion. Fig. 8a reveals a bright field STEM image of the as-extruded TZA353 alloy, and the electron beam direction is parallel to $[0001]_{\alpha}$ zone axis. The spherical distribution of the

second phase particles shows an obvious mass thickness contrast with the size between 50 and 400nm. Combined with the EDS analysis shown in Fig. 8b, the particles with dark contrast are Mg_2Sn and those with grey contrast are I-phase. In addition, we found that large number of Mg_2Sn particles with size below 50nm are attached to the I-phase particles, as shown in the green dotted rectangle in Fig. 8a and the HAADF-STEM image in Fig. 8c. The SAED pattern of corresponding area in Fig. 8c suggests that there is no obvious orientation relationship between I phase and Mg_2Sn. In addition, the nature of the interface between the second phase particles and matrix is one of the important factors affecting the strengthening mechanism of alloys. Therefore, it is necessary to discuss the interface coherency relationship between I-phase particle and surrounding α-Mg matrix in the present study. A HAADF-STEM image of an I-phase particle with composition near $Mg_{47}Zn_{28}Al_{25}$ are shown in Fig. 8d, and the electron beam is parallel to $[5\text{-fold}]_I$ symmetry axis. Accordingly, the HR-TEM micrograph of the interface region between this I-phase particle and α-Mg matrix exhibited in Fig. 8e, and corresponding FFT patterns are obtained from the regions marked by area1 and area2, respectively. The FFT pattern obtained from the area1 shows that this I-phase particle has a five-fold rotational symmetry structure. Simultaneously, the fringes of the α-Mg matrix planes can be observed clearly in the interface region, and the crystalline interplanar spacing between them is 0.244nm, which correspond to the $(10\bar{1}1)$ plane in hcp structure. The $(10\bar{1}1)$ plane and five-fold symmetry (5f) oriented along the [5-fold] axis are marked in Fig. 8e, and corresponding diffraction spots are marked in the FFT pattern obtained from the area2. Combined with the above results, HR-TEM micrograph and FFT patterns in Fig. 8(e-f) show an orientation relationship which can be expressed as $\{10\bar{1}1\}_\alpha$//5f with a slight misorientation (~6°). Same type of coherency orientation relationship has been reported in Mg-Zn-Y alloy system which can be expressed as $[2\text{-fold}]_I$//$[0001]_{\alpha\text{-Mg}}$, and 2f ,5f//$\{10\bar{1}0\}_{\alpha\text{-Mg}}$, indicating that atomic scale bonding between the I-phase and the hexagonal structure is rigid enough to be retained during the severe plastic deformation [32]. This type of rigid interface between I-phase and α-Mg matrix may play an important role in enhancing the strength and formability of alloy [22].

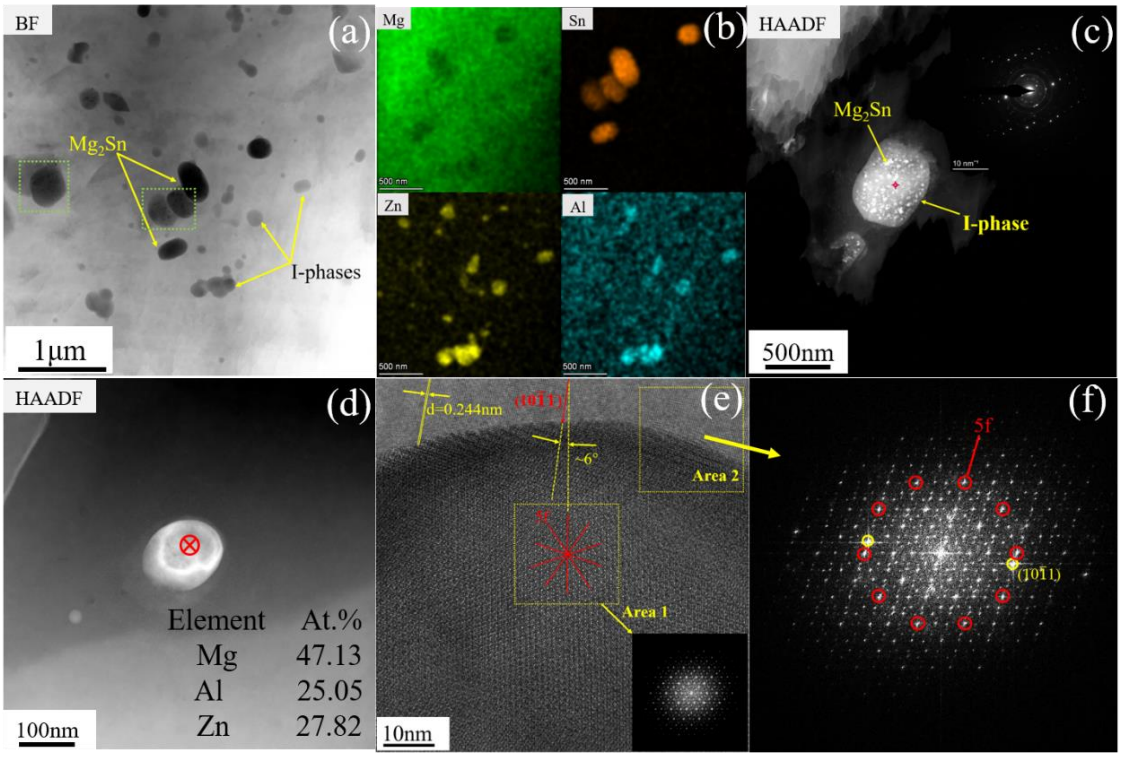

Fig. 8. STEM and HR-TEM micrographs of as-extruded TZA353 alloy: (a-b) Bright field STEM micrograph and corresponding EDS mapping result; (c) HAADAF-STEM image shows the phenomenon that a few nano-sized Mg_2Sn adhere to the I-phase particle and corresponding SAED pattern inserted in (c); (d-e) HADDF-STEM and HR-TEM micrograph of the I-phase particle which has a five-fold rotational symmetry structure. The FFT patterns in (e) and (f) are obtained from the region marked by area1 and area2 in (e).

On the other hand, we found a new kind of secondary phase with crystal structure in as-extruded TZA353 alloy. A HAADF-STEM image and corresponding EDS result as shown by Fig. 9a exhibit a particle with composition near $Mg_{51}Zn_{25}Al_{24}$ and size about 180nm. The HR-TEM micrograph and the corresponding FFT pattern shown in Fig. 9b-c identify the particle as φ-phase, which possesses a primitive orthorhombic unit cell [33]. As marked in Fig. 9b, the crystalline interplanar spacing of d_1 and d_2 are 0.864nm and 1.658nm respectively, which correspond to the (001) and (020) plane in the primitive orthorhombic structure, and the electron beam direction is parallel to the $[\bar{1}00]_{\varphi}$. It was pointed out that [34] there are great similarities in composition and structure between the φ-phase and the I-phase, and the icosahedral clusters are also found in the unit cell of the φ-phase. Therefore, it can be explained that some ternary phases tend to form the crystal structure of φ phase favorably rather than all of quasicrystal I-phase during the extrusion process. It's also possible that part of the I-phase had been transformed into φ-phase during the homogenization treatment. This hypothesis is based on the experimental results reported by early researches [29, 35, 36], and its accuracy needs further study.

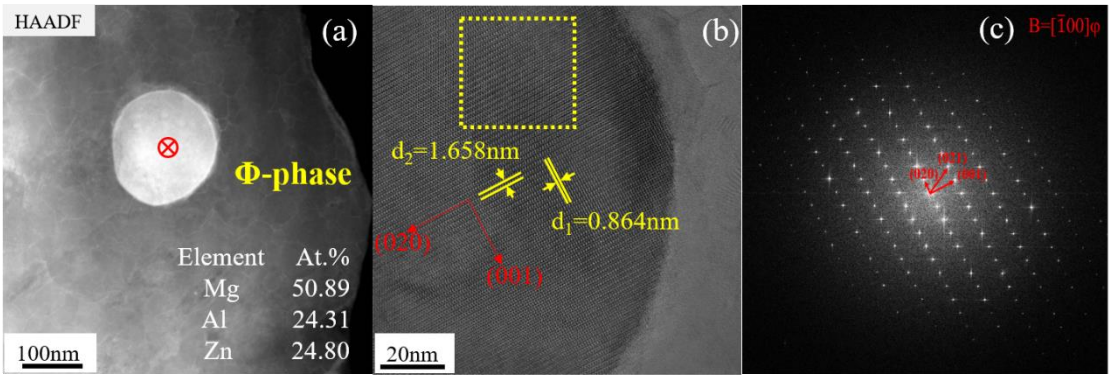

Fig. 9. STEM and HR-TEM images showing a new kind of secondary phase in as-extruded TZA353 alloy: (a) HADDF-STEM and corresponding EDS result of a φ-phase particle; (b) HR-TEM images of the φ-phase particle; (c) FFT pattern of the marked area in (b).

Fig. 10 presents the EBSD results of Band Contrast (BC) images and distribution mappings of different kinds of grain in as-extruded TZ35, TZA351, TZA353 alloy, respectively. The blue area represents recrystallized grains, the yellow area represents sub-grains, and the red area represents deformed grains. As observed in BC images, the microstructure of as-extruded alloys is composed of almost complete recrystallization grains and secondary phases which were crushed into streamlined fragments in the extrusion process. The volume fraction of DRX grains in TZ35 alloy accounts for more than 99%, while it declined slightly with the addition of Al, and a small minority of deformed regions and substructures appeared. At the same time, the average grain size of the alloy is considerably refined from the initial 9.9μm (in TZ35 alloy) to 3.1μm (in TZA353 alloy).

In general, magnesium alloys get fully recrystallized microstructure when the extrusion temperature exceeds 350°C [2]. Although the extrusion temperature was at 300°C in this experiment, the fully dynamic recrystallization was promoted due to the fact that additional friction heat and deformation heat would be generated during hot extrusion [12, 37], making the actual temperature higher than 300°C. Besides, alloying element also affects the DRX behavior during hot deformation process. The addition of Sn and Zn significantly reduced the stacking fault energy of the α-Mg matrix [38-40], which made the dynamic recrystallization easy to occur during the hot extrusion process. The primary factor of grain refinement in as-extruded alloys was attributed to the DRX behavior promoted by the large number of streamlined particles (as observed in Fig.10) through the particle-stimulated nucleation (PSN) mechanism and shear bands (labeled as region a, b and c in Fig 10c) caused by localized deformation. It is considered that those streamlined particles and flow localizations provided more nucleation sites for dynamic recrystallization grains by accumulating high density dislocations in the vicinity of the particles during hot deformation [41, 42], and thus promoting the DRX grain refinement. As a result, DRX grains near the streamlined particle area are considerably finer than those far away from the particle region, as shown in TZA351 and TZA353

alloys (Fig. 10b and c). In addition, quite a few studies pointed out [43, 44] nano-sized secondary phase particles (<1μm) may lead to Zener grain-boundary pinning effect, hence hindering recrystallization nucleation and grain growth. In this study, both the dynamic precipitation of Mg_2Sn and nano-size secondary precipitates (as shown in Fig. 7) hindered the DRX through the Zener pinning effect, thus leading to a slight decrease in the volume fraction of the DRX region with the rising of Al content.

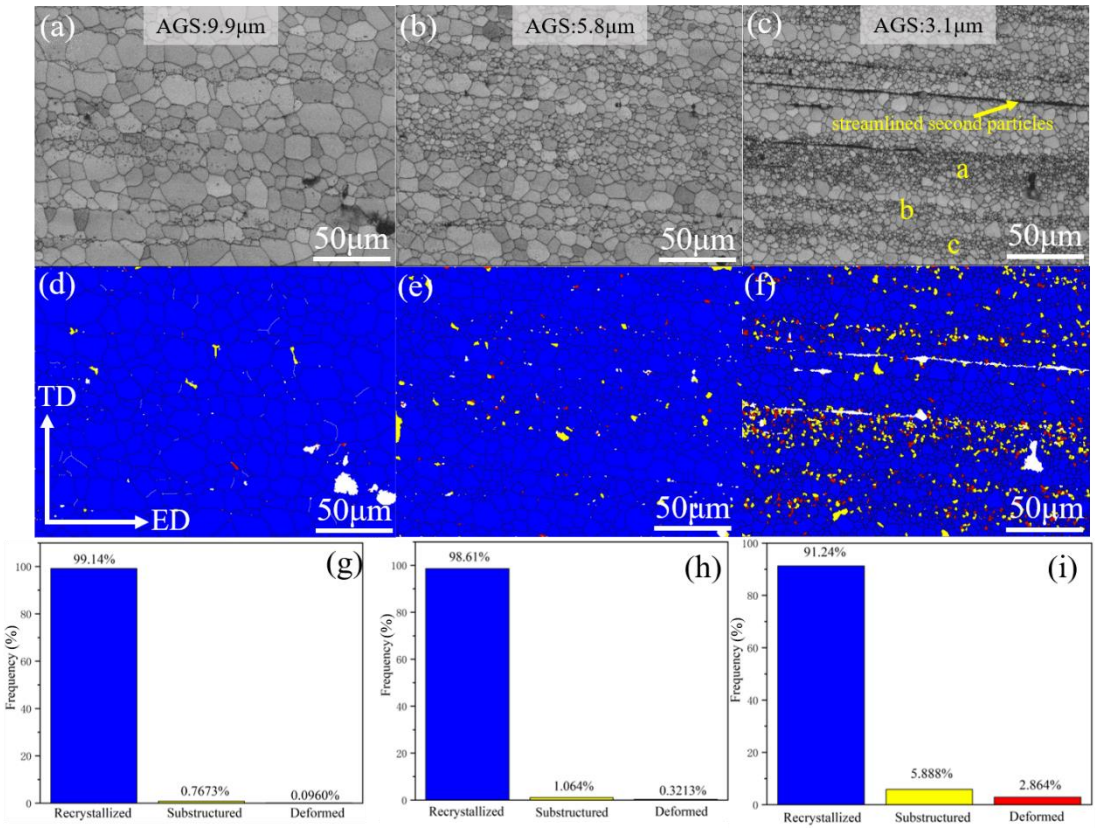

Fig. 10 EBSD results of Band Contrast (BC) images and distribution mappings of different kinds of grain in as-extruded (a, d) TZ35 alloy, (b, e) TZ351 alloy, (c, f) TZ353 alloy. Blue-recrystallized regions, yellow-substructured regions, red-deformed regions; (g), (h) and (i) are the statistical frequency of different types of grain regions in (d), (e) and (f), respectively. AGS denotes the average grain size of as-extruded alloys.

Fig. 11 shows the IPF maps, pole figures and misorientation angle distributions of as-extruded alloys, which help us further understand the evolution of texture and grain orientation after extrusion. Different colors in IPF maps represent different grain orientations, and their actual orientation refers to the inserted legend of IPF map in Fig. 11a. Clearly, most of grains in IPF maps present green and blue color, indicating that the <01$\bar{1}$0>and <$\bar{1}$2$\bar{1}$0> axes of those grains are parallel to the extrusion direction (ED). Combined with pole figures, specifically, TZ35 alloy formed a relatively strong basal texture with the maximum intensity of 8.02, as shown by {0001} pole figure in Fig. 11a. Moreover, the average angle θ between c-axis and ED in TZ35 alloy is about 80°, indicating that the c-axes are nearly perpendicular to the ED. With the addition of Al content, the basal texture of

TZA351 and TZA353 was obviously weakened, and the maximum intensity is about 5.45 and 5.51, respectively. Besides, the c-axes of most grains deflect into the transverse direction (TD), and the angle θ between c-axis and ED decreases with the Al addition. Significantly, the critical resolved shear stress (CRSS) required to activate the basal slip largely depends on the Schmidt factor (SF) value of the basal <a> slip, which is closely related to the angle θ between the c-axis and the loading direction. Relevant literature pointed out that [13] the SF value for basal slip increases with increasing θ when $0 < \theta < 45$ °. Meanwhile, the basal <a>slip and $\{10\bar{1}2\}$ twinning dominate the main deformation mode [45]. Nevertheless, SF value for basal slip decreases gradually with increasing θ when $45 < \theta < 90$ °. Especially when the θ is close to 90°, the non-basal slips are the dominant deformation mode [46]. As shown by pole figures in Fig. 11b-c, the angles θ between c-axis and ED in TZA351 and TZA353 range from 60° to 75°, which are universally smaller than that in TZ35. Therefore, it can be inferred that SF value for the basal slip increased with the addition of Al and the basal texture was weakened, which can be confirmed in pole figures and subsequent analysis in Fig. 12. In addition, the white lines in the IPF maps represent the low angle grain-boundaries (LAGBs) with misorientation angle between 2° and 15°, which generally appear in deformed grains region, leading to the highest frequency of the LAGBs in TZA353 alloy followed by TZA351 and TZ35 successively, confirmed by Fig.11d-f.

In order to investigate the main deformation mechanism of as-extruded alloy during the tensile deformation in this experiment, Fig. 12 reveals the Schmid factor maps and distribution for basal <a> slip, prismatic <a>slip, and pyramidal <c+a> slip of as-extruded alloys, respectively. As depicts in these maps, the average SF value for basal<a>slip in TZ35 is relatively lower than that for prismatic <a> slip and pyramidal <c+a> slip, which are between 0.4 and 0.5, indicating that non-basal slip dominates the major deformation mode in as-extruded TZ35 alloy. On the other hand, the average SF value for non-basal slip in TZA351 and TZA353 did not change significantly with the addition of Al, whereas it seems to increase slightly for basal slip. It suggests that the critical resolved shear stress (CRSS) required to activate the basal slip decreases, which means easier to activate the basal slip in TZA351 and TZA353 alloy. But non-basal slip is still the main deformation mode. Activation of non-basal slip in as-extruded alloys probably attribute to the following factors: Firstly, high volume fraction of DRX fine grains makes the dislocation slip shorter and the deformation more homogenous, and fine grains would decrease the CRSS difference between basal and non-basal systems [2]. Secondly, GB compatibility stresses boost the cross-slip of basal <a> dislocations to non-basal planes during tensile deformation [47]. Thirdly, properly dissolved Zn (no more than 1.0 at.%) may reduce the CRSS anisotropy between basal and non-basal slip systems, which is beneficial to activating non-basal slip systems [48]. Therefore, the above-mentioned factors

may give rise to the activation of non-basal slip, which may significantly improve the ductility of as-extruded alloys.

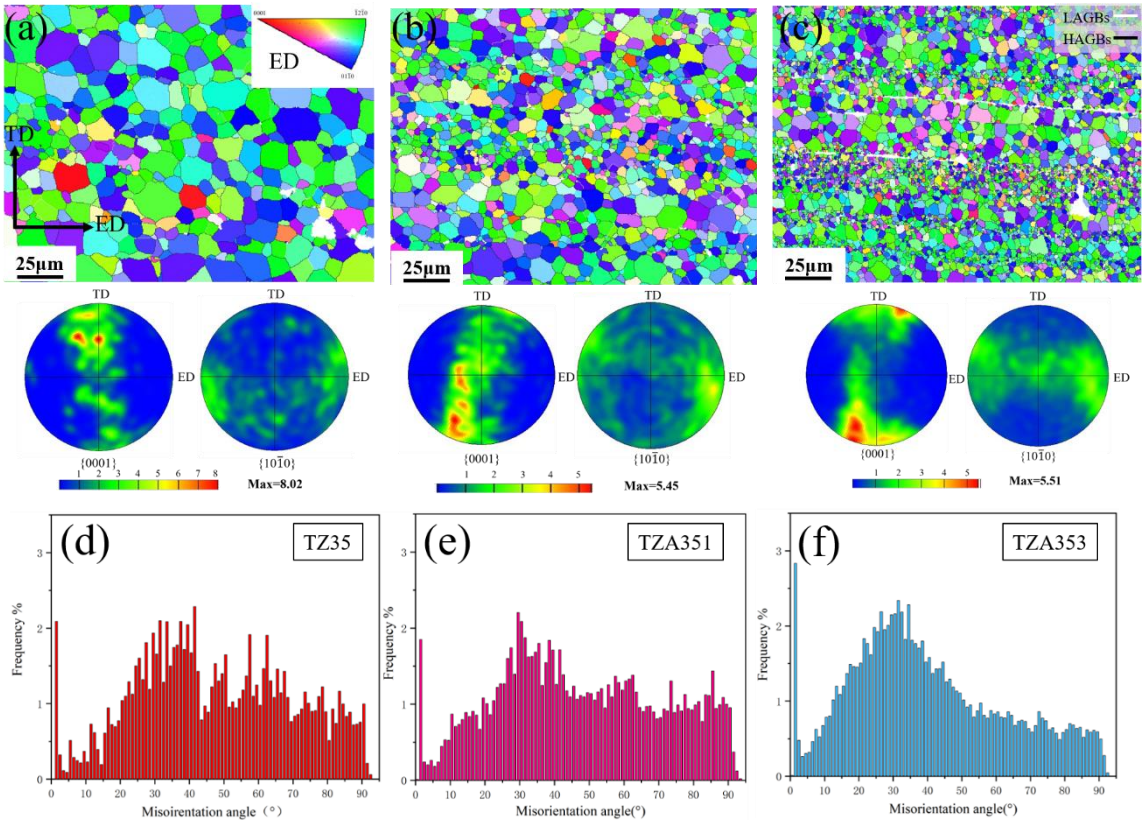

Fig. 11. Inverse pole figure (IPF) maps, pole figures with the maximum intensity and corresponding misorientation angle distributions of as-extruded (a) and (d) TZ35 alloy, (b) and (d) TZA351 alloy, (e) and (f) TZA353 alloy, respectively.

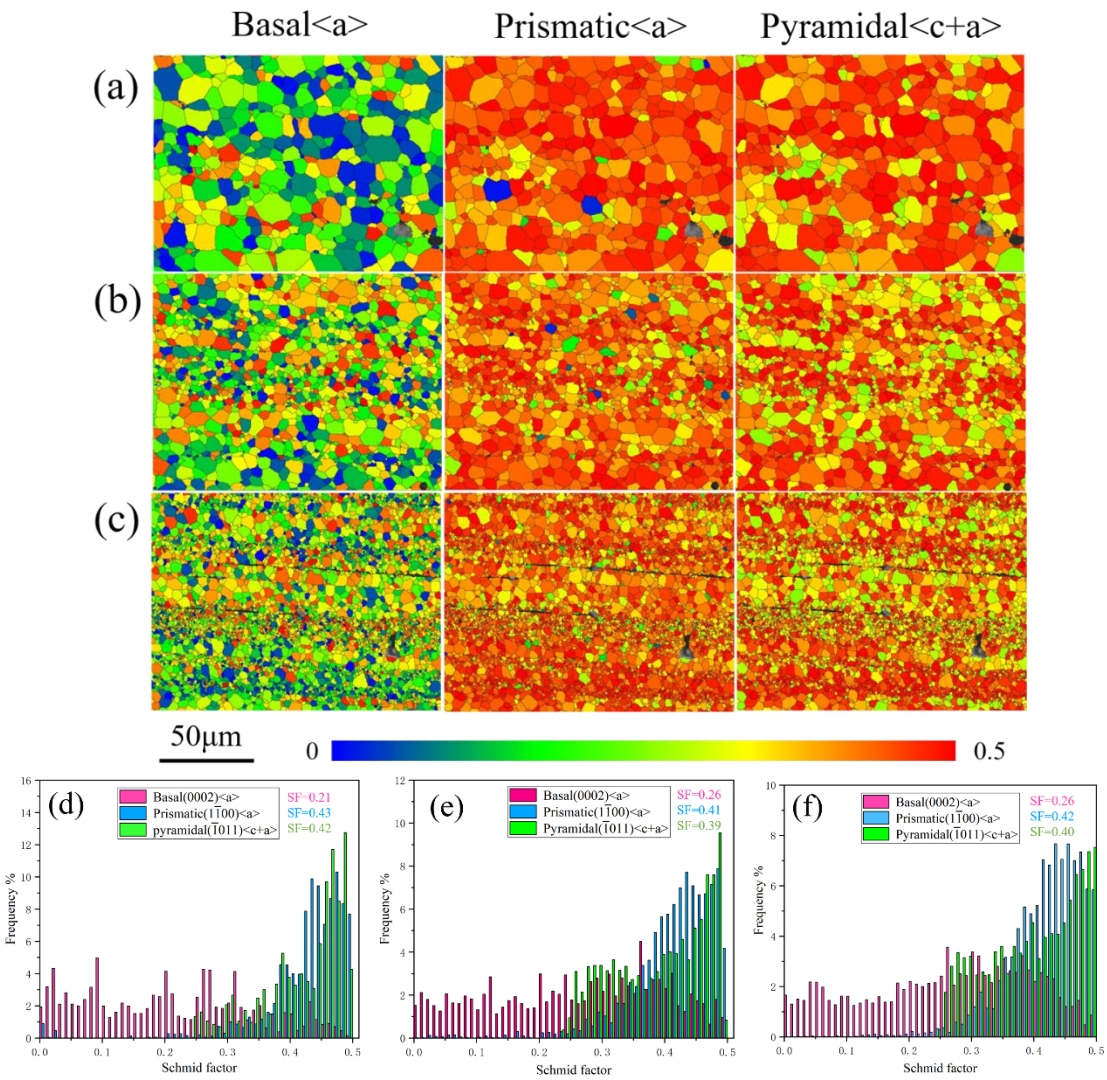

Fig. 12. Schmid factor maps and distribution for (0002)/ <11$\bar{2}$0> basal slip, {1$\bar{1}$00}/ <11$\bar{2}$0> prismatic slip, and {$\bar{1}$011}/ <11$\bar{2}$3> pyramidal slip of as-extruded TZ35 (a, d), TZA351 (b, e), and TZA353 (c, f) alloy, respectively.

3.4 Mechanical properties of as-extruded alloys

Fig. 13 shows the engineering stress-strain curves of the as-extruded alloys at room temperature. Corresponding mechanical properties and grain size are listed in Table 3. The results show that the yield strength of as-extruded alloys increased dramatically with the addition of Al, and TZA353 reaches the highest yield strength of 212 MPa, which is 25.4% higher than that of TZ35 alloy, whereas TZA351 alloy has the highest ultimate tensile strength and elongation, reaching 340 MPa and 20.1% respectively. Subsequently, ultimate tensile strength shows a trend of decreasing and then rising with increasing Al content, while the elongation gradually decreased.

Alloys	YS (MPa)	UTS (MPa)	Elongation (%)	Grain size/μm
TZ35	169±4.1	306±2.5	19.4±1.7	9.90
TZA351	188±3.6	340±2.7	20.1±1.2	5.85
TZA352	203±4	328±2.6	18.0±0.7	4.68
TZA353	212±2.3	336±3.2	15.5±1.0	3.11

Table 3 Mechanical properties and grain size of the as-extruded alloys at room temperature.

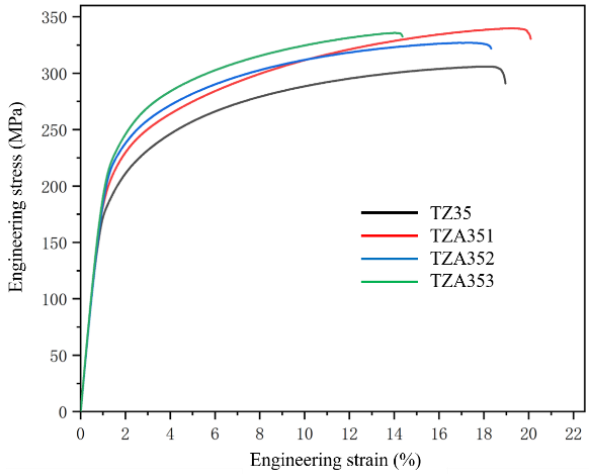

Fig. 13. The engineering stress-strain curves for tensile test of as-extruded alloys at room temperature.

There are many factors affecting the mechanical properties of as extruded alloys, such as grain size, second phase particles, texture and so on. Based on the characterization results, grain boundary strengthening and precipitation strengthening of the second phase particles played crucial roles in enhancing the strength of the alloy.

Grain boundary strengthening through fine DRX grains dramatically contributed to the yield strength enhancement. According to the Hall-Petch relationship [49], grain boundary strengthening effect can be estimated as follows：

$$\sigma_y = \sigma_0 + k_y d^{-1/2} \quad (1)$$

Where σ_y is yield stress, σ_0 represents the lattice resistance to dislocation motion, d is the average grain size. k_y is the Hall-Petch coefficient, which is related to the lattice structure, grain size, and texture, etc [50]. As shown in Fig. 10, the grain size of the as-extruded alloys decreases gradually with the addition of Al element, and the measured average grain size of the as-extruded TZ35-xAl (x=0,1,2,3) alloys are 9.9μm, 5.85μm, 4.68μm, and 3.11μm, respectively. By assuming that all the as-extruded alloys in the present study share the same σ_0 and k_y values. Therefore, the yield strength increment due to grain refinement by addition of Al can be calculated as follow:

$$\Delta\sigma = k_y \left(d_{TZ35-xAl(x=1,2,3wt.\%)}^{-1/2} - d_{TZ35}^{-1/2}\right) \quad (2)$$

On the basis of previous research [49], the k_y value at present study is 290 MPa $\mu m^{-1/2}$. Hence, compared with the TZ35 alloy, the increments of yield strength caused by grain refinement in

as-extruded TZ35-xAl (x=1,2,3) alloys are 27 MPa, 41 MPa, and 72 MPa, respectively. Moreover, the second phase is another indispensable factor that may affect the strength of as-extruded alloy. As shown in Fig. 7, massive secondary phase particles dispersedly distributed in the α-Mg matrix, which strongly inhibited the movement of dislocations, leading to improvement of the strength. It is generally accepted that the Mg_2Sn and nano-size I-phase particles are two kinds of hard and brittle phases, which are not easy to deform during loading. Hence dislocation cutting mechanism may be inappropriate for the present alloy system. Besides, the rigid interface between I-phase particle and the surrounding α-Mg matrix can provide an enhanced strengthening effect following the Orowan process [32]. Therefore, it is considered that the Orowan mechanism is responsible for interpretation of the precipitation hardening in as-extruded alloys. According to the Orowan strengthening equation, the strengthening effect of the second phase particles is closely related to the average particle size and the mean spacing of second phase particles. The equations can be expressed as follow [51]:

$$\sigma_{Orowan}=\frac{0.13Gb}{\lambda}ln\frac{dp}{2b} \quad (3)$$

$$\lambda = dp[(\frac{1}{2fp})^{1/3} - 1] \quad (4)$$

Where dp is the average size of the particles, b is the Burgers vector (3.21×10^{-10}m), and G is the shear modulus (16.6 GPa). λ is the mean spacing between particles. If the particles are randomly distributed in the matrix, λ value can be calculated according to the equation (4). where fp represents the volume fraction of second phase particles. To some extent, the higher the volume fraction of the second phase particles, the smaller the mean spacing between particles, which may lead to higher precipitate strengthening effect. According to the equations (3) and (4), in the present study, the theoretical calculation results of precipitate strengthening effect in as-extruded alloys are shown in Table 4. Thus, compared with TZ35, $\Delta\sigma_{\mathrm{Orowan}}=2.5$MPa, 1.3MPa and 4.75 MPa, respectively.

Alloy	f_p (%)	d_p (μm)	λ (μm)	σ_{Orowan} (MPa)
TZ35	9.8	0.5	0.368	12.5
TZA351	12.1	0.5	0.308	15.0
TZA352	13.4	0.6	0.349	13.8
TZA353	15.2	0.6	0.263	18.1

Table 4 Theoretical calculation of the precipitate strengthening effect in as-extruded TZ35-xAl alloys.

Based on the above theoretical calculation results, compared with TZ35, the yield strength increments $\Delta\sigma_y$ of as-extruded TZ35-xAl (x=1,2,3) alloy are 29.5MPa, 42.3MPa and 77.6MPa, respectively, which are much higher than actual tested $\Delta\sigma_y =$ 19MPa, 34MPa and 43MPa. it is

supposed that the weakened texture caused by the addition of Al may reduce the yield strength of the as-extruded alloys.

Unlike the yield strength, ultimate tensile strength (UTS) shows the tendency to increase first and then decline (Table 3). When the Al content is added up to 2wt.% or 3wt.%, the undissolved Mg-Zn-Al ternary phase is too coarse (as shown in Fig. 7), which may not hinder the dislocations effectively. On the contrary, coarse secondary phase would increase stress concentration and become the crack sources under loading, and thus deteriorating the mechanical properties of the alloys. Compared with TZA352 and TZA353, TZA351 alloy has less coarse secondary phase and more uniform microstructure. That's why the UTS of the TZA352 and TZA353 are inferior to TZA351.

Except for strength, excellent ductility for as-extruded alloys is mainly ascribed to the activation of non-basal slip systems and large volume fraction of fine DRX grains, which made the deformation more uniform. Moreover, weakened texture and refinement of grains due to the Al addition also contribute to improving the ductility. The fracture morphology of tensile specimens was characterized by SEM (as shown in Figure 14) to further investigate the ductility in as-extruded alloy. Compared with TZ351, the volume fraction of dimples in TZA352 and TZA353 alloys is decreased, and cleavage planes with river pattern and more broken coarse second phase can be observed in some areas. The results show that the fracture mode of the as-extruded alloys transit from ductile fracture to brittle fracture, and the cracks would propagate along the river pattern of cleavage plane and the stress concentration area caused by the coarse secondary phase during loading. Consequently, the increase in the volume fraction of coarse secondary phases and cleavage planes may be responsible for the inferior ductility in TZA352 and TZA353.

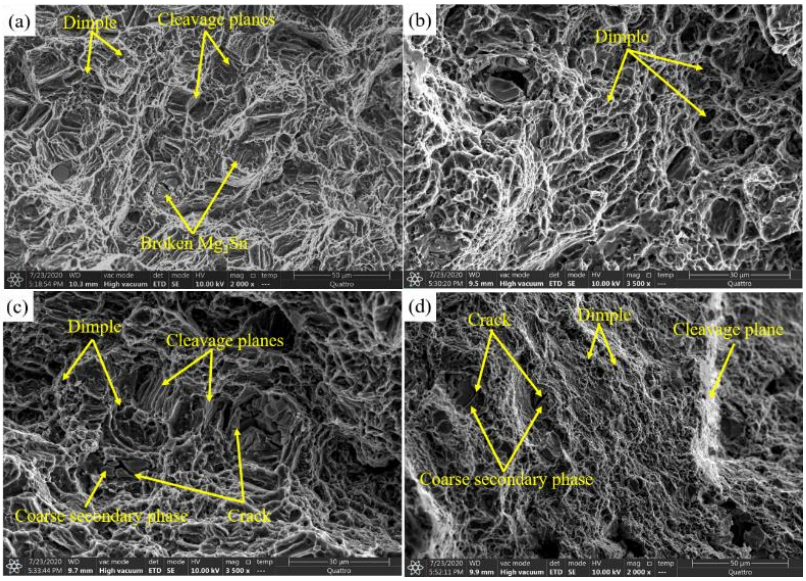

Fig. 14 SEM images for tensile fracture morphology of as-extruded TZ35-xAl alloys: (a)TZ35; (b) TZA351;(c) TZA352;(d) TZA353.

4.Conclusion

In this study, a series of rare-earth free Mg-3Sn-5Zn-xAl (x=0,1,2,3 wt.%) alloys were prepared and the effects of Zn/Al mass ratio on microstructure evolution and mechanical properties of the as-cast and as-extruded alloys were systematically investigated. A few important conclusions obtained as following:

1. The second phase of as-cast alloys transformed from $MgZn_2$/α-Mg eutectics and Mg_2Sn to icosahedral (I-) phases and Mg_2Sn in the wake of decreasing of Zn/Al mass ratio. I-phase and Mg_2Sn exhibit excellent thermal stability during the homogenization treatment.

2. The average grain size of as-extruded TZ35-xAl alloys was considerably refined with the increasing of Al content. Almost fully recrystallized microstructure was obtained in TZ35-xAl alloy, but the volume fraction of recrystallized region was slightly reduced by the addition of Al. This phenomenon was chiefly ascribed to the particle-stimulated nucleation (PSN) mechanism (particle size>1μm) and Zener grain-boundary pinning effect (nano-size) induced by enormous numbers of Mg-Zn phase, I-phase, Mg_2Sn and newly formed φ-phase (related with I-phase) particles.

3. Compared with TZ35, Al-containing alloys exhibited weaker basal texture and the angle θ between c-axis and ED decreased, leading to higher SF value for basal<a>slip. However, the average SF value for non-basal slip in Al-containing alloys did not change obviously, which were much higher than that for basal<a>slip, indicating non-basal slip was still the main deformation mechanism of as-extruded alloys during tensile deformation.

4. As-extruded TZ35-xAl alloys exhibited superior strength and ductility balance. Improved tensile yield strength was primarily attributed to the synergistic reinforcement mechanism of grain refinement and precipitation of secondary particles. The excellent ductility owes a great deal to the activation of non-basal slip systems, high volume fraction of fine DRX grains and weakened texture. Nevertheless, TZA352 and TZA353 alloys contained a few undissolved coarse phases, which may cause stress concentration and become the crack sources during the tensile deformation, and thus resulting in inferior UTS and ductility. Meanwhile, decreasing in volume fraction of dimples and observed cleavage planes indicate that the rupture of the as-extruded alloys transformed from ductile fracture to brittle fracture.

Acknowledgement

This research was supported by the National Key Research and Development Program of China [grant numbers:2016YFB0301100], and Chongqing technology innovation and application development project, China [grant numbers: cstc2019jscx-dxwtB0029].

References

[1] Y. Ali, D. Qiu, B. Jiang, F. Pan, M.-X. Zhang, Current research progress in grain refinement of cast magnesium alloys: A review article, Journal of Alloys and Compounds 619 (2015) 639-651.
[2] J. Song, J. She, D. Chen, F. Pan, Latest research advances on magnesium and magnesium alloys worldwide, Journal of Magnesium and Alloys 8 (2020) 1-41.
[3] H. Pan, Y. Ren, H. Fu, H. Zhao, L. Wang, X. Meng, G. Qin, Recent developments in rare-earth free wrought magnesium alloys having high strength: A review, Journal of Alloys and Compounds 663 (2016) 321-331.
[4] C.L. Mendis, K. Oh-ishi, K. Hono, Enhanced age hardening in a Mg–2.4at.% Zn alloy by trace additions of Ag and Ca, Scripta Materialia 57(6) (2007) 485-488.
[5] T. Nakata, C. Xu, H. Ohashi, Y. Yoshida, K. Yoshida, S. Kamado, New Mg–Al based alloy sheet with good room-temperature stretch formability and tensile properties, Scripta Materialia 180 (2020) 16-22.
[6] J. Zhang, S. Liu, R. Wu, L. Hou, M. Zhang, Recent developments in high-strength Mg-RE-based alloys: Focusing on Mg-Gd and Mg-Y systems, Journal of Magnesium and Alloys 6(3) (2018) 277-291.
[7] T.T. Sasaki, K. Oh-ishi, T. Ohkubo, K. Hono, Enhanced age hardening response by the addition of Zn in Mg–Sn alloys, Scripta Materialia 55(3) (2006) 251-254.
[8] F.R. Elsayed, T.T. Sasaki, T. Ohkubo, H. Takahashi, S.W. Xu, S. Kamado, K. Hono, Effect of extrusion conditions on microstructure and mechanical properties of microalloyed Mg–Sn–Al–Zn alloys, Materials Science and Engineering: A 588 (2013) 318-328.
[9] A. Dev, N. Naskar, N. Kumar, A. Jena, M. Paliwal, A systematic investigation of secondary phase dissolution in Mg–Sn alloys, Journal of Magnesium and Alloys 7(4) (2019) 725-737.
[10] W.L. Cheng, S.S. Park, B.S. You, B.H. Koo, Microstructure and mechanical properties of binary Mg-Sn alloys subjected to indirect extrusion, Mat Sci Eng a-Struct 527(18-19) (2010) 4650-4653.
[11] W.N. Tang, S.S. Park, B.S. You, Effect of the Zn content on the microstructure and mechanical properties of indirect-extruded Mg–5Sn–xZn alloys, Materials & Design 32(6) (2011) 3537-3543.
[12] S.-H. Kim, J.U. Lee, Y.J. Kim, J.-G. Jung, S.H. Park, Controlling the microstructure and improving the tensile properties of extruded Mg-Sn-Zn alloy through Al addition, Journal of Alloys and Compounds 751 (2018) 1-11.
[13] S.-H. Kim, S.H. Park, Underlying mechanisms of drastic reduction in yield asymmetry of extruded Mg-Sn-Zn alloy by Al addition, Materials Science and Engineering: A 733 (2018) 285-290.
[14] R.G. Li, Y. Xu, W. Qi, J. An, Y. Lu, Z.Y. Cao, Y.B. Liu, Effect of Sn on the microstructure and compressive deformation behavior of the AZ91D aging alloy, Materials Characterization 59(11) (2008) 1643-1649.
[15] M.L. Olguín-González, D. Hernández-Silva, M.A. García-Bernal, V.M. Sauce-Rangel, Hot deformation behavior of hot-rolled AZ31 and AZ61 magnesium alloys, Materials Science and Engineering: A 597 (2014) 82-88.
[16] W.L. Xiao, Y.S. Shen, L.D. Wang, Y.M. Wu, Z.Y. Cao, S.S. Jia, L.M. Wang, The influences of rare earth content on the microstructure and mechanical properties of Mg-7Zn-5Al alloy, Materials & Design 31(7) (2010) 3542-3549.
[17] M.B. Yang, F.S. Pan, Effects of Sn addition on as-cast microstructure, mechanical properties and casting fluidity of ZA84 magnesium alloy, Materials & Design 31(1) (2010) 68-75.
[18] B. Wang, X. Chen, F. Pan, J. Mao, Effects of Sn addition on microstructure and mechanical properties of Mg-Zn-Al alloys, Progress in Natural Science: Materials International 27(6) (2017) 695-

702.
[19] Y. Zhang, X. Huang, Z. Ma, Y. Li, F. Guo, J. Yang, Y. Ma, Y. Hao, The influences of Al content on the microstructure and mechanical properties of as-cast Mg-6Zn magnesium alloys, Materials Science and Engineering: A 686 (2017) 93-101.
[20] S. Harosh, L. Miller, G. Levi, M. Bamberger, Microstructure and properties of Mg–5.6%Sn–4.4%Zn–2.1%Al alloy, Journal of Materials Science 42(24) (2007) 9983-9989.
[21] S.-L.C. H. LIANG, and Y.A. CHANG, A Thermodynamic Description of the Al-Mg-Zn System, METALLURGICAL AND MATERIALS TRANSACTIONS A 28A (1997) 1725-1734.
[22] Y.K. Kim, S.W. Sohn, D.H. Kim, W.T. Kim, D.H. Kim, Role of icosahedral phase in enhancing the strength of Mg–Sn–Zn–Al alloy, Journal of Alloys and Compounds 549 (2013) 46-50.
[23] G. BERGMAN., J.L.T. WAUGH., L. PAULING., Crystal Structure of the lntermetallic Compound Mg_{32} (Al,Zn) $_{49}$ and Related Phases, NATURE 169 (1952) 1057-1058.
[24] B. Bokhonov., I. Konstanchuk., E. Ivanov., V. Boldyrev., Stage formation of quasi-crystals during mechanical treatment of the cubic Frank-Kasper phase Mg32(Zn, A1)49, Journal of Alloys and Compounds 187 (1992) 207-214.
[25] A. Smontara, I. Smiljanić, A. Bilušić, Z. Jagličić, M. Klanjšek, S. Roitsch, J. Dolinšek, M. Feuerbacher, Electrical, magnetic, thermal and thermoelectric properties of the “Bergman phase” Mg32(Al,Zn)49 complex metallic alloy, Journal of Alloys and Compounds 430(1-2) (2007) 29-38.
[26] Z.Z. Shi, W.Z. Zhang, Investigation on the microstructure of a τ-Mg32(Al, Zn)49strengthened Mg–Zn–Al alloy with relatively low Zn content, Phase Transitions 85(1-2) (2012) 41-51.
[27] M. Vogel, G.D. O. Kraft*, E. Arzt, Quasi-crystalline grain-boundary phase in the magnesium die-cast alloy ZA85, Scripta Materialia 45 (2001) 517-524.
[28] J. Zhang, Z.X. Guo, F. Pan, Z. Li, X. Luo, Effect of composition on the microstructure and mechanical properties of Mg–Zn–Al alloys, Materials Science and Engineering: A 456(1-2) (2007) 43-51.
[29] H. Somekawa, Y. Osawa, A. Singh, T. Mukai, Rare-earth free wrought-processed magnesium alloy with dispersion of quasicrystal phase, Scripta Materialia 61(7) (2009) 705-708.
[30] J. ZHANG, F. PAN, Z.X.GUO, Development of a T-type Mg-Zn-Al Alloy:An investigation of the Microstructure and solidification characteristics, Materials Science Forum 546-d549 (2007) 123-128.
[31] Y.a. Chen, Y. Wang, J. Gao, Microstructure and mechanical properties of as-cast Mg-Sn-Zn-Y alloys, Journal of Alloys and Compounds 740 (2018) 727-734.
[32] D.H. Bae, S.H. Kim, D.H. Kim, W.T. Kim, Deformation behavior of Mg–Zn–Y alloys reinforced by icosahedral quasicrystalline particles, Acta Materialia 50 (2002) 2343–2356.
[33] P. Donnadieu, A. Quivy, T. Tarfa, P. Ochin, A. Dezellus, M.G. Harmelin, P. Liang, H.L. Lukas, H.J. Seifert, F. Aldinger, G. Effenberg, On the crystal structure and solubility range of the ternary phi phase in the Mg-Al-Zn system, Zeitschrift Fur Metallkunde 88(12) (1997) 911-916.
[34] L. BOURGEOIS, B. C. MUDDLE, J.F. NIE, The crystal structure of the equilibrium Φ phase in Mg–Zn–Al casting alloys, Acta Materialia 49(14) (2001) 2701-2711.
[35] Y.P. Ren, G.W. Qin, W.L. Pei, Y. Guo, H.D. Zhao, H.X. Li, M. Jiang, S.M. Hao, The α-Mg solvus and isothermal section of Mg-rich corner in the Mg–Zn–Al ternary system at 320°C, Journal of Alloys and Compounds 481(1-2) (2009) 176-181.
[36] J.-F. Nie, Precipitation and Hardening in Magnesium Alloys, Metallurgical and Materials Transactions A 43(11) (2012) 3891-3939.
[37] J.G. Jung, S.H. Park, B.S. You, Effect of aging prior to extrusion on the microstructure and

mechanical properties of Mg-7Sn-1Al-1Zn alloy, Journal of Alloys and Compounds 627 (2015) 324-332.
[38] D. Luo, H.-Y. Wang, L. Chen, G.-J. Liu, J.-G. Wang, Q.-C. Jiang, Strong strain hardening ability in an as-cast Mg-3Sn-1Zn alloy, Materials Letters 94 (2013) 51-54.
[39] S. Huang, J.F. Wang, F. Hou, Y. Li, F.S. Pan, Effect of Sn on the formation of the long period stacking ordered phase and mechanical properties of Mg-RE-Zn alloy, Materials Letters 137 (2014) 143-146.
[40] H. Yu, H.Y. , J.C. , B.S. , Y.Z. , Y.S. , Z.M. , Effects of minor Gd addition on microstructures and mechanical properties of the high strain-rate rolled Mg–Zn–Zr alloys, Journal of Alloys and Compounds 586 757–765 (2014).
[41] J.D. Robson, D.T. Henry, B. Davis, Particle effects on recrystallization in magnesium–manganese alloys: Particle-stimulated nucleation, Acta Materialia 57(9) (2009) 2739-2747.
[42] Y. Chai, B. Jiang, J. Song, Q. Wang, H. Gao, B. Liu, G. Huang, D. Zhang, F. Pan, Improvement of mechanical properties and reduction of yield asymmetry of extruded Mg-Sn-Zn alloy through Ca addition, Journal of Alloys and Compounds 782 (2019) 1076-1086.
[43] S.H. Park, J.-G. Jung, Y.M. Kim, B.S. You, A new high-strength extruded Mg-8Al-4Sn-2Zn alloy, Materials Letters 139 (2015) 35-38.
[44] W. Cheng, Y. Bai, L. Wang, H. Wang, L. Bian, H. Yu, Strengthening Effect of Extruded Mg-8Sn-2Zn-2Al Alloy: Influence of Micro and Nano-Size Mg_2Sn Precipitates, Materials (Basel) 10(7) (2017).
[45] H. Liao, J. Kim, T. Liu, A. Tang, J. She, P. Peng, F. Pan, Effects of Mn addition on the microstructures, mechanical properties and work-hardening of Mg-1Sn alloy, Materials Science and Engineering: A 754 (2019) 778-785.
[46] B. Song, R.L. Xin, N. Guo, T.T. Liu, Q.S. Yang, Research progress of strain hardening behavior at room temperature in wrought magnesium alloys, Zhongguo Youse Jinshu Xuebao/Chinese Journal of Nonferrous Metals 24(11) (2014) 2699-2710.
[47] J. Koike, T. Kobayashi, T. Mukai, H. Watanabe, M. Suzuki, K. Maruyama, K. Higashi, The activity of non-basal slip systems and dynamic recovery at room temperature in fine-grained AZ31B magnesium alloys, Acta Materialia 51(7) (2003) 2055-2065.
[48] Hyo-Sun Jang, B.-J. Lee, Effects of Zn on ⟨c+a⟩ slip and grain boundary segregation of Mg alloys, Scripta Materialia 160 39–43 (2019).
[49] H. Yu, Y. Xin, M. Wang, Q. Liu, Hall-Petch relationship in Mg alloys: A review, Journal of Materials Science & Technology 34(2) (2018) 248-256.
[50] W. Yuan, S.K. Panigrahi, J.Q. Su, R.S. Mishra, Influence of grain size and texture on Hall–Petch relationship for a magnesium alloy, Scripta Materialia 65(11) (2011) 994-997.
[51] T.Y. Kwak, W.J. Kim, Mechanical properties and Hall-Petch relationship of the extruded Mg-Zn-Y alloys with different volume fractions of icosahedral phase, Journal of Alloys and Compounds 770 (2019) 589-599.